21. We estimated the precision of the GPS baseline vectors by adjusting the two surveys for common coordinates. The solution covariance matrices obtained from the GPS processing software were then scaled so that the weighted residual sum of squares divided by the number of degree of freedom was 1.0.
22. W. Thatcher, *U.S. Geol. Surv. Prof. Pap. 1515* (1991), p. 189.
23. Following the methods of P. Segall and M. V. Mathews [*J. Geophys. Res.* **93**, 14954 (1988)].
24. R. A. Snay, J. F. Ni, H. C. Neugebauer, in preparation.
25. J. C. Savage and R. O. Burford, *Bull. Seismol. Soc. Am.* **60**, 1877 (1970).
26. O. W. Nuttli, *ibid.* **73**, 519 (1983).
27. D. P. Russ, *U.S. Geol. Surv. Prof. Pap. 1236* (1982), p. 95.
28. In possible contradiction with the results presented in (*3*) (*27*), no evidence of paleoliquefaction effects was found in a series of drainage ditches in the southern NMSZ (S. G. Wesnousky and L. M. Leffler, in preparation). However, the absence of paleoliquefaction features does not demonstrate that prehistoric earthquakes did not occur.
29. Analysis of crustal deformation data just north of the San Francisco Bay by W. Prescott and S.-B. Yu [*J. Geophys. Res.* **91**, 7475 (1986)] indicates that right-lateral slip on the San Andreas fault and several subparallel right-lateral strike slip fault zones result from lower crustal ductile deformation distributed over a zone approximately 50 km wide.
30. E. S. Schweig III and R. T. Marple, *Geology* **19**, 1025 (1991).
31. W. M. Elsasser, in *The Application of Modern Physics to the Earth and Planetary Interiors*, S. K. Runcorn, Ed. (Wiley-Interscience, New York, 1969), pp. 223–244.
32. W. Thatcher, *J. Geophys. Res.* **88**, 5893 (1983).
33. For example, seismic reflection profiling in the New Madrid area has revealed remarkably little deformation of the unconformity between Paleozoic bedrock and Upper Cretaceous through Cenozoic Coastal Plain sediments (*8*); R. M. Hamilton and M. D. Zoback, *U.S. Geol. Surv. Prof. Pap. 1236* (1982)], p. 55.
34. In Table 1, the uncertainties are 1 SD, based on the a priori data errors. $\sigma_0$ refers to the a posteriori SD of an observation of a priori unit weight (*2, 3*) [also see, for example, R. Snay, *J. Geophys. Res.* **91**, 12695 (1986)]. We calculated a posteriori SDs by multiplying the SEs in Table 1 by $\sigma_0$. Confidence intervals of 95% for $\dot{\gamma}$ were estimated by Monte Carlo simulation. Gaussian random variables with means equal to observed values of $\dot{\gamma}_1$ and $\dot{\gamma}_2$ and variances equal to the a posteriori variances were drawn to simulate $\dot{\gamma}$ according to Eq. (*1*). An independent analysis of the data from the western subnetwork by R. Snay of the NGS yielded essentially the same strain rate as presented in Table 1.
35. We thank W. H. Prescott and M. Lisowski for help with this study, and R. A. Snay for cooperation. A. Johnston and J. Savage made useful comments on an earlier version of this manuscript. This work was supported by U.S. Geological Survey grant 14-08-0001-G1943-02.

17 March 1992; accepted 15 July 1992

# Exsolution of Hornblende and the Solubility Limits of Calicum in Orthoamphibole

Eugene A. Smelik and David R. Veblen

**Exsolution between orthorhombic and monoclinic amphibole has been postulated for many years on the basis of crystal-chemical and structural differences. Transmission and analytical electron microscope examination of calium-rich gedrite specimens from southwestern New Hampshire has now revealed evidence for exsolution of calcic clinoamphibole (hornblende) from ferromagnesian orthoamphibole. Analytical electron microscopy data suggests that calcium has a low solubility limit in the orthoamphibole structure. The hornblende lamellae range from only a few unit cells in thickness to about 80 nanometers. The formation of the calcic amphibole lamellae resulted from heterogeneous nucleation and growth along pre-existing (100) stacking faults. Thus, the deformation processes producing the stacking faults played a key role in preparing the sites for exsolution.**

Exsolution, sometimes called phase separation, unmixing, or precipitation, is a common and important process that occurs in a wide range of natural and synthetic solid solutions. Precipitation hardening is a primary method of strengthening in many metal alloy systems, especially in aluminum and magnesium alloys (*1*). Exsolution is equally important in glass and glass-ceramic systems for purposes of strengthening and purification (*2*). Controlling exsolution reactions and thus the characteristics of the resulting microstructures in metal, glass, and glass-ceramic systems allows for the production of many materials possessing a wide range of desirable properties.

Exsolution occurs in a wide range of natural mineral systems, especially the oxides and silicates. Exsolution microstructures in minerals not only change the mineral's physical properties, but they also serve as a record of the postcrystallization mineral behavior. The characterization of exsolution microstructures in silicate mineral systems has provided a more complete understanding of the crystal chemistry and behavior of complex, multicomponent solid solutions. In addition, exsolution microstructures are potentially useful tools for unraveling pressure-temperature-time histories of igneous and metamorphic rocks. The increased use of transmission and analytical electron microscopy (TEM/AEM) in mineralogy in recent years has provided much new evidence for exsolution in many silicate systems, such as feldspars, pyroxenes, amphiboles, and micas (*3*). Moreover, TEM/AEM techniques allow for the detailed crystallographic and crystal-chemical characterization of fine-scale precipitates and in many instances provide clues for the exsolution mechanisms responsible for the microstructures. Results from such studies are especially useful in that reaction rates of many silicate exsolution reactions are too slow to study in the laboratory. In this report we provide evidence for exsolution between two members of the amphibole mineral group (double-chain silicates), specifically between ferromagnesian orthorhombic amphiboles in the anthophyllite-gedrite series and the monoclinic calcic amphibole, hornblende.

In the analogous pyroxene system (single-chain silicates), it is common for ferromagnesian orthopyroxenes to contain exsolution lamellae of the Ca-rich clinopyroxene augite along (100) (*4*). Because of the close chemical and structural similarities between pyroxenes and amphiboles, one would expect that similar exsolution phenomena should occur between calcic clinoamphiboles and orthoamphiboles. Despite the abundance of orthoamphibole-bearing rocks from high-grade metamorphic terranes and numerous studies of coexisting orthoamphiboles and clinoamphiboles, such exsolution microstructures have not been reported (*5*).

Using TEM and AEM (*6*), we examined *Pnma* orthoamphibole samples from the "Amphibole Hill" area of southwestern New Hampshire (*7*). The orthoamphiboles come from sillimanite-staurolite grade amphibolites consisting primarily of coexisting, coarse-grained hornblende and orthoamphibole (*8*). Visible light microscopy of the coarse hornblende crystals shows abundant exsolution lamellae of primitive, $P2_1/m$ cummingtonite along (100) and $(\bar{1}01)$ (*9*), whereas the orthoamphiboles appear to be homogeneous.

When examined with the electron microscope, the orthoamphiboles were found to be completely exsolved; they consist of coherently intergrown lamellae of anthophyllite and gedrite. The orthoamphibole exsolution lamellae have orientations that range from (010) to (120) (*10, 11*). Punctuating the anthophyllite-gedrite exsolution texture are lamellae of hornblende reaching maximum thicknesses of 60 to 80 nm (Fig. 1). The hornblende lamellae appear to be coherently intergrown exactly along (100) as shown by the [001] high-resolution TEM (HRTEM) image shown in

E. A. Smelik, Department of Geological and Geophysical Sciences, Guyot Hall, Princeton University, Princeton, NJ 08544.
D. R. Veblen, Department of Earth and Planetary Sciences, Johns Hopkins University, Baltimore, MD 21218.

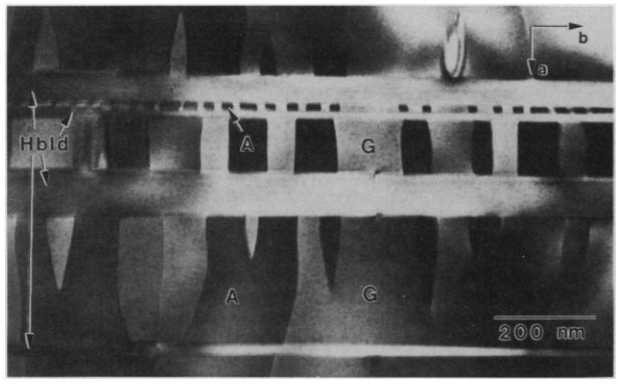


**Fig. 1.** Bright-field TEM image of (100) hornblende exsolution lamellae (Hbld) in orthoamphibole host. Later generations of anthophyllite lamellae (A) in gedrite (G) have nucleated heterogeneously along the hornblende lamellar interfaces, growing between adjacent hornblende lamellae. Some of the larger anthophyllite and gedrite lamellae can be traced across the hornblende lamellae, suggesting that they predated the formation of the clinoamphibole. The electron beam is parallel to the *c* axis.

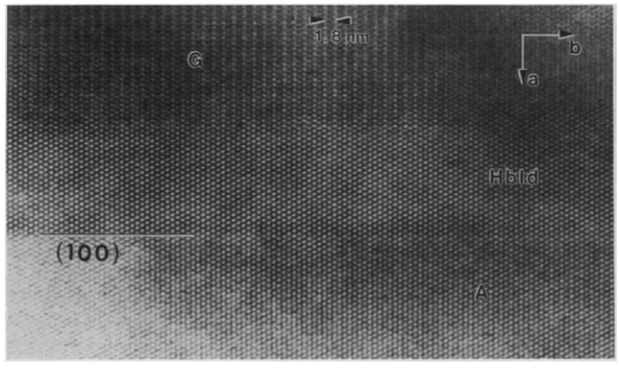


**Fig. 2.** High-resolution TEM (HRTEM) image taken down the *c* axis, showing a coherent section of interface between orthoamphibole (A,G) and clinoamphibole (Hbld) along (100). It is likely that the hornblende nucleated along a pre-existing (100) stacking fault, which is common in orthoamphiboles. Misfit dislocations have been observed along the interfaces of these exsolution lamellae when tilted out of this [001] orientation.

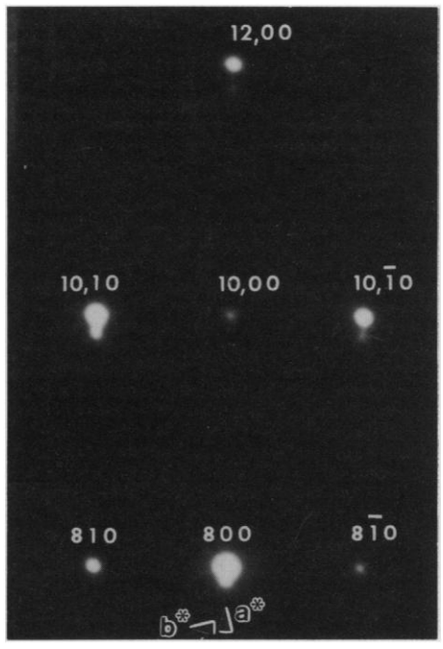


**Fig. 3.** An enlarged portion of a [001] selected-area electron diffraction (SAED) pattern showing the $a^*$-$b^*$ reciprocal lattice plane. The (12,00), (10,10), (10,00), (10,$\bar{1}$0), (810), (800), and (8$\bar{1}$0) orthoamphibole reflections are labeled. The corresponding clinoamphibole reflections are (600), (510), (500), (5$\bar{1}$0), (410), (400), and (4$\bar{1}$0), respectively. Note the splitting along $a^*$, reflecting the difference in $a$ axial lengths between hornblende and the orthoamphibole. Also note that the splitting, that is, the appearance of hornblende reflections, only occurs for diffraction spots that satisfy the condition $h + k = 2n$ for the *C2/m* clinoamphibole lattice [for example, (510)] and are absent for reflections of the type $h + k = 2n + 1$ [for example, (500)].

Fig. 2. However, misfit dislocations were often seen when tilting the specimen out of this orientation by a significant amount (20° to 30°), and hence the lamellae are semicoherent. The interface may be considered to be an optimal phase boundary between the clinoamphibole and orthoamphibole structures that results primarily from the relatively large difference in the magnitude of the $a$ axes between hornblende and orthoamphibole (Fig. 3) and the structural similarities between the monoclinic and orthorhombic amphibole structures along (100). To confirm the C2/*m* symmetry for the hornblende lamellae, dark-field TEM images of hornblende-containing areas were obtained utilizing the 600 diffracted reflection. This reflection satisfies the condition $g = (h + k)/2 = 2n + 1$, for which the 600 reflection in the *Pnma* orthoamphibole lattice corresponds to the forbidden 300 reflection in the C2/*m* clinoamphibole lattice. In such images, the hornblende lamellae are black; this result confirms that the amphibole is monoclinic. The systematically absent reflections for the clinoamphibole C-centered cell are also apparent in the enlarged electron diffraction pattern shown in Fig. 3. This pattern is a portion of the $a^*$-$b^*$ reciprocal lattice plane and shows the (12,00), (10,10), (10,00), (10,$\bar{1}$0), (810), (800), and (8$\bar{1}$0) orthoamphibole reflections. These same reflections, in terms of the clinoamphibole cell, are (600), (510), (500), (5$\bar{1}$0), (410), (400), and (4$\bar{1}$0), respectively. Splitting of the reflections due to the difference in $a$ axial lengths of hornblende and orthoamphibole occurs only for hornblende reflections of the type $h + k = 2n$ [for example, (510)], and the $h + k = 2n + 1$ hornblende reflections [for example, (500)] are absent, as is consistent with C2/*m* space-group symmetry.

We obtained energy-dispersive x-ray analyses of the hornblende lamellae using a fine electron beam (10 to 20 nm) (*12*). In addition, bulk orthoamphibole analyses were collected by rastering a large, diffuse beam over the exsolved areas near, but not immediately adjacent to, the hornblende lamellae (Table 1).

Because the hornblende lamellae are small and widely scattered throughout the host, the bulk orthoamphibole composition (Table 1) closely approximates the pre-hornblende exsolution composition. One may imagine that exsolution occurs when the homogeneous parent mineral, which crystallized at high temperature, slowly cools. Unmixing likely follows by cation diffusion which can be described by one or more cation exchange vectors. These exchange vectors, when applied to the host composition, lead to the composition of the exsolved phase (*13*).

As shown in Table 1, the hornblende lamellae show increases in Ti, $Al^{VI}$, $Al^{IV}$, $Na^{M4}$, and Ca; and decreases in Fe, Mg, and Mn compared to the orthoamphibole host. These chemical changes can be achieved by invoking the following four amphibole cation exchange vectors: Titschermakite ($TiA^{IV}{}_2Mg_{-1}Si_{-2}$), tschermakite ($Al^{VI}Al^{IV}Mg_{-1}Si_{-1}$), glaucophane ($Na^{M4}Al^{VI}Ca_{-1}Mg_{-1}$), and cummingtonite ($Ca[Fe, Mg, Mn]_{-1}$). Because the estimated *A*-site contents for both the clinoamphibole and bulk orthoamphibole are essentially the same (Table 1), the edenite exchange, $Na^{A}Al^{IV}\square_{-1}Si_{-1}$, does not operate during the hornblende exsolution.

By comparing the idealized site occupancies shown in Table 1, the dominant chemical change during hornblende exsolution is the cummingtonite exchange, which involves only the M4 crystallographic site and

**Table 1.** Average AEM data for hornblende (hbld), lamellae (lam.), and orthoamphibole (oam) host in sample 6A9S from Amphibole Hill. Also shown are the average compositions of the gedrite (ged) and anthophyllite (anth) exsolution lamellae taken from (*11*). Amphibole compositions are calculated on a 23-oxygen basis with all Fe as FeO.

| Cation or site | hbld lam. | bulk oam | anth lam. | ged lam. |
|---|---|---|---|---|
| Si | 6.41 | 6.71 | 7.76 | 6.18 |
| $Al^{IV}$ | 1.59 | 1.29 | 0.24 | 1.82 |
| ΣT site | 8.00 | 8.00 | 8.00 | 8.00 |
| $Al^{VI}$ | 0.99 | 0.65 | 0.04 | 1.11 |
| Ti | 0.10 | 0.04 | 0.01 | 0.02 |
| Mg | 2.98 | 4.18 | 4.75 | 3.60 |
| Fe | 1.07 | 1.89 | 1.96 | 1.93 |
| Mn | 0.02 | 0.11 | 0.12 | 0.13 |
| Ca | 1.70 | 0.13 | 0.06 | 0.12 |
| $Na^{M4}$ | 0.15 | 0.00 | 0.06 | 0.09 |
| ΣM sites | 7.00 | 7.00 | 7.00 | 7.00 |
| $Na^{A}$ | 0.52 | 0.53 | 0.23 | 0.75 |
| K | 0.03 | 0.01 | 0.01 | 0.00 |
| ΣA site | 0.55 | 0.54 | 0.24 | 0.75 |
| Fe/(Fe + Mg) | 0.264 | 0.312 | 0.292 | 0.349 |

is consistent with the major chemical discontinuity between the calcic and ferromagnesian amphibole groups. Other amphibole-coupled substitutions involving the M4, M2, and T sites are also important during this exsolution process, however.

Bulk AEM analyses of the orthoamphibole show that actual Ca contents range from 0.11 to 0.15 atoms per formula unit (pfu) (approximately 0.75 to 1.0% CaO by weight). The appearance of exsolution lamellae at such low concentrations of Ca suggests that the solubility limit for Ca in the orthoamphibole structure is low. Indeed, there have been few reports of orthoamphibole containing greater than 0.1 Ca atoms pfu (*5*, *14*). On the basis on the our results, it is likely that the few reported Ca-rich orthoamphiboles are either exsolved or are intimate mixtures of ferromagnesian and calcic amphiboles.

Figure 4 shows a plot of Ca contents versus Fe/(Fe + Mg) ratio for the orthoamphibole compositions from this sample. For the exsolved orthoamphibole pairs, anthophyllite is always lower in both Fe/(Fe + Mg) and Ca than coexisting gedrite (Fig. 4). This implies that the gedrite structure is more tolerant of Ca than the anthophyllite structure under identical conditions of *P* and *T*.

In the analogous pyroxene system, Robinson (*15*) has shown that orthopyroxenes are also relatively intolerant of Ca. Deer *et al.* (*16*) reported Ca contents in orthopyroxenes that ranged from very low (0.008 ions pfu or 0.23% CaO by weight) to a Ca-rich bronzite that contains 0.162 Ca ions pfu, or 4.19% CaO by weight (cations calculated on a six-oxygen basis). Many orthopyroxenes contain optically visible (100) lamellae of Ca-clinopyroxene, and it seems likely that optically homogeneous orthopyroxenes containing significant Ca may be exsolved at the nanometer scale, similar to these orthoamphiboles.

Stacking faults along (100) are common in orthoamphiboles (*10*, *11*, *19*). These faults are essentially narrow, one- or two-unit-cell slabs of clinoamphibole structure within the orthoamphibole, and they are usually attributed to deformation. The (100) hornblende lamellae always form along (100) stacking faults in the Amphibole Hill amphiboles. These faults serve as perfect structural templates for the C2/*m* clinoamphibole structure and provide an easy pathway for heterogeneous nucleation and growth of hornblende lamellae. Thus, the deformation process producing the stacking faults sets the stage for the exsolution reactions to proceed during slow cooling from the peak metamorphic temperature. Exsolution of hornblende may be further enhanced by the presence of anthophyllite lamellae, which are less tolerant of Ca than gedrite; the hornblende therefore exsolve to accommodate the increased Ca concentration. Growth of hornblende lamellae proceeds by the formation of growth ledges similar to those described for exsolved pyroxenes (*20*).

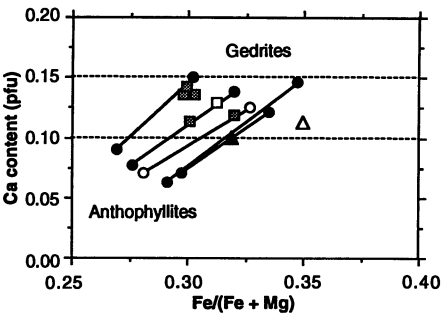


**Fig. 4.** Plot of Ca content versus Fe/(Fe + Mg) for orthoamphiboles from sample 6A9S. The filled circles connected by tie-lines are exsolved pairs taken from (*11*). The open circles connected by a tie-line represent the average anthophyllite and gedrite lamellar compositions (average of 25 AEM analyses per mineral), also from (*11*). The anthophyllites are always lower in Ca and Fe/(Fe + Mg) ratio. The stippled squares are typical bulk orthoamphibole compositions determined by AEM. The open square is the average bulk orthoamphibole composition (from ten AEM analyses, see Table 1). For comparison, the open triangle is the wet chemical composition 6A9X given by Robinson *et al.* (*17*) for 6A9 orthoamphiboles, and the filled triangle is an electron microprobe composition 6A9S from Schumacher (*18*) for these orthoamphiboles. The region bracketed by dashed lines between Ca values of 0.10 and 0.15 is meant to represent the approximate solubility limits for Ca in bulk, unexsolved orthoamphibole in this bulk compositional range.

If the orthoamphiboles had been free of stacking faults, or other defects, exsolution of Ca-amphibole probably would not have occurred in these samples, because of the higher activation energy needed for homogeneous nucleation and growth, or perhaps would have occurred with higher degrees of undercooling below the solvus temperature.

## REFERENCES AND NOTES


1. R. E. Reed-Hill, *Physical Metallurgy Principles* (Prindle, Weber, and Schmidt, Boston, MA, 1973).
2. W. D. Kingery, H. K. Brown, D. R. Uhlmann, *Introduction to Ceramics* (Wiley, New York, ed. 2, 1976).
3. For examples of recent exsolution studies using TEM/AEM see: for feldspars, W. L. Brown and I. Parsons, *Phys. Chem. Mineral.* **10**, 55 (1983); for pyroxenes, K. J. T. Livi, *Contrib. Mineral. Petrol.* **96**, 371 (1987); for amphiboles, E. A. Smelik, M. W. Nyman, D. R. Veblen, *Am. Mineral.* **76**, 1184 (1991); for micas, E. A. Ferrow, D. London, K. S. Goodman, D. R. Veblen, *Contrib. Mineral. Petrol.* **105**, 491 (1990).
4. See, for example: P. E. Champness and G. W. Lorimer, *J. Mater. Sci.* **8**, 467 (1973); G. W. Lorimer and P. E. Champness, *Am. Mineral.* **58**, 243 (1973); J. B. Vander Sande and D. L. Kohlstedt, *Philos. Mag.* **29**, 1041 (1974).
5. P. Robinson *et al.*, in *Amphiboles: Petrology and Experimental Phase Relations*, D. R. Veblen and P. H. Ribbe, Eds. (Mineralogical Society of America, Washington, DC, 1982), pp. 1–227.
6. Samples for TEM study were prepared by ion-thinning selected areas of petrographic thin sections. Electron microscopy was performed with a Philips EM 420 equipped with a SuperTwin objective lens, and operated at 120 keV.
7. This amphibole locality, known as outcrop 6A9, has been described by P. Robinson *et al.* [*Mineral. Soc. Am. Spec. Pap. 2*, 251 (1969)] and J. C. Schumacher and P. Robinson [*Field Trip Guidebook: Regional Metamorphism and Metamorphic Phase Relations in Northwestern and Central New England*, P. Robinson and D. C. Elbert, Eds. (14th General Meeting, International Mineralogical Association, Contrib. 59, the Department of Geology and Geography, University of Massachusetts, Amherst, 1986), pp. 145–194].
8. The amphibolites from locality 6A9 also contain intermediate plagioclase and traces of biotite, chlorite, ilmenite, and apatite. R. J. Tracy, P. Robinson, and A. B. Thompson [*Am. Mineral.* **61**, 762 (1976)] estimated that the amphiboles crystallized at 625° to 650°C and ~6 kbar.
9. The structure of the cummingtonite exsolution lamellae in the coarse hornblendes was determined by M. Ross, J. J. Papike and K. W. Shaw, [*Mineral. Soc. Am. Spec. Pap. 2* (1969), p. 275].
10. M. F. Gittos, G. W. Lorimer, P. E. Champness, in *Electron Microscopy in Mineralogy*, H.-R. Wenk *et al.*, Eds. (Springer-Verlag, Berlin, 1976), pp. 238–247. These authors noted the presence of (100) stacking faults in their TEM study of similarly exsolved orthoamphiboles from Amphibole Hill but they were unable to obtain any compositional data that might suggest they were very narrow lamellae of hornblende.
11. E. A. Smelik, thesis, Johns Hopkins University, Baltimore, MD (1991); D. R. Veblen, in preparation.
12. The energy-dispersive x-ray spectra were collected with an EDAX Si(Li) detector and processed with a Princeton Gamma-Tech model 4000 analyzer, as described by K. J. T. Livi and D. R. Veblen [*Am. Mineral.* **72**, 113 (1987)]. We recalculated all amphibole analyses to a 23-oxygen basis following the method of Robinson *et al.* (*5*), assuming all Fe to be present as FeO. AEM analyses are of inherently poorer quality compared to electron microprobe analyses, especial-

ly for Na, because of Na loss in the beam and low detection efficiency. Furthermore, additional statistical analytical errors are usually introduced when analyzing small precipitates because the overall count rates are much lower than for coarse areas.
13. The vector treatment of amphibole compositions is discussed by J. B. Thompson, Jr., in *Characterization of Metamorphism through Mineral Equilibria*, J. M. Ferry, Ed. (Mineralogical Society of America, Washington, DC, 1982), pp. 1–32.
14. J. C. Rabbitt [*Am. Mineral.* **33**, 263 (1948)] published two anthophyllite compositions showing 0.50 and 0.49 Ca pfu (analyses #15 and 41); W. A. Deer, R. A. Howie, and J. Zussman [*Rock-Forming Minerals, vol. 2, Chain Silicates* (Longmans, Green, London, 1963), pp. 211–229] reported an anthophyllite with 0.492 Ca pfu (analysis #1); and G. N. Starkov [*Zap. Vses. Mineral. Obhch.* **101**, 349 (1972)] published an anthophyllite analysis containing 0.569 Ca pfu.
15. P. Robinson, in *Pyroxenes*, C. T. Prewitt, Ed. (Mineralogical Society of America, Washington, DC, 1980), pp. 419–494.
16. W. A. Deer, R. A. Howie, J. Zussman, *Rock-Forming Minerals*, vol. 2A, *Single-Chain Silicates* (Wiley, New York, 1978), pp. 41, Table 4, analysis #5.
17. P. Robinson, M. Ross, H. Jaffe, *Am. Mineral.* **56**, 1005 (1971).
18. J. C. Schumacher, personal communication.
19. P. J. Treloar and A. Putnis, *Mineral. Mag.* **45**, 55 (1982).
20. D. L. Kohlstedt and J. B. Vander Sande, in *Electron Microscopy in Mineralogy*, H.-R. Wenk *et al.*, Eds. (Springer-Verlag, Berlin, 1976), pp. 234–237.
21. We thank J. Schumacher for supplying a chip of orthoamphibole from locality 6A9 and for providing unpublished microprobe analyses. We also thank P. J. Heaney and M. W. Nyman for reviewing the manuscript. The electron microscopy was undertaken at the transmission electron microscope facility in the Department of Earth and Planetary Sciences at The Johns Hopkins University, Baltimore, MD, supported by National Science Foundation grant EAR89-03630 and instrumentation grant EAR83-00365.

21 May 1992; accepted 20 July 1992

# Responses to Elevated Carbon Dioxide in Artificial Tropical Ecosystems

Christian Körner* and John A. Arnone III

**Carbon, nutrient, and water balance as well as key plant and soil processes were simultaneously monitored for humid tropical plant communities treated with $CO_2$-enriched atmospheres. Despite vigorous growth, no significant differences in stand biomass (of both the understory and overstory), leaf area index, nitrogen or water consumption, or leaf stomatal behavior were detected between ambient and elevated $CO_2$ treatments. Major responses under elevated $CO_2$ included massive starch accumulation in the tops of canopies, increased fine-root production, and a doubling of $CO_2$ evolution from the soil. Stimulated rhizosphere activity was accompanied by increased loss of soil carbon and increased mineral nutrient leaching. This study points at the inadequacy of scaling-up from physiological baselines to ecosystems without accounting for interactions among components, and it emphasizes the urgent need for whole-system experimental approaches in global-change research.**

Greater carbon sequestering by terrestrial ecosystems, increasing amounts of leaf area per unit of land area, reduced water consumption, and greater efficiency of mineral nutrient capture are some of the common predictions for plant and ecosystem behavior in a future world with high levels of $CO_2$ (*1–5*). We evaluated these assumptions in an experiment with closed ecosystems of tropical rain forest plants of various life forms arranged in complex communities.

The only available data about in situ $CO_2$ responses of a natural terrestrial ecosystem, Alaskan tundra (*6*), revealed no such growth stimulation, whereas semiaquatic salt-marsh vegetation, whose nutritional situation is comparable to agricultural conditions, not surprisingly showed positive biomass responses similar to those found in crops (*7, 8*). Forests, which make up about 90% of the global biomass, have not yet been studied under artificially enhanced $CO_2$ levels, and current predictions of their behavior in a $CO_2$-rich world are based on data largely derived from experiments with isolated seedlings (*4, 9*). Before success is realized from long-term and large-scale $CO_2$ enrichment experiments on natural forests (*10*), investigations with experimental ecosystems provide an excellent means for the assessment of $CO_2$ effects in highly structured ecosystems. We selected a humid tropical ecosystem because this biome represents about 40% of the global biomass and because plant responses to $CO_2$ are predicted to be more pronounced under high temperatures (*11*).

We constructed four such model ecosystems by enclosing identically structured populations of 15 tropical plant species (*12*) in 17-$m^3$ polyethylene-covered houses. Plants in each house shared a common soil volume of 1.3 $m^3$ and ground area of 6.7 $m^2$. The two to six individuals of each species in each ecosystem were located in exactly the same position in the four houses. Soils consisted of a mixture of silicate sand and vermiculite, overlain by a thin layer of leaf and bark compost, which was supplemented with 20 g per square meter of timed-release fertilizer pellets. Houses were situated in a climate-conditioned greenhouse at the University of Basel, Switzerland, and received natural daylight. Closed air-circulation systems changed the air in each house 11 times per hour and included activated charcoal filters and dew point and temperature controllers with dehumidifying water traps. The experimental ecosystems were not designed to mimic a specific natural situation but to represent model stands with a characteristic vertical stratification.

All ecosystems were allowed to stabilize under low $CO_2$ levels (340 μl of $CO_2$ per liter of air) for 30 days before the experiment. No differences in stand structure {for example, leaf area index [LAI; area of leaves ($m^2$) per square meter of ground] and mean height of individual plants} were apparent among houses after this stabilization period. Daytime $CO_2$ was maintained at 340 μl of $CO_2$ per liter in two of the houses, while the other two received 610 μl of $CO_2$ per liter during the experiment. The experiment was terminated after 3 months, 1 month after the LAI stabilized at a value typical for humid tropical forests (*13*).

Total ecosystem biomass at both $CO_2$ levels more than doubled within 3 months (from about 700 to 1500 g of dry mass per square meter); thus, the experimental conditions supported vigorous growth. Despite this increase, neither the biomass of the entire ecosystem nor that of the individual species (*14*) responded significantly to elevated $CO_2$ (Table 1), although a slight positive effect was detected. This result is in contrast to that of Ziska *et al.* (*15*), who reported dramatic stimulation of growth in tropical plants isolated in pots that contained rich soil. However, in the long run, marginal gains, such as those found here under elevated $CO_2$, could still result in more rapid maturation of stands.

One of the key determinants of carbon fixation by ecosystems is the amount of photosynthetic machinery per unit area of land, commonly expressed as the LAI. Elevated $CO_2$ has been shown to enable plants to achieve greater relative carbon gains under low irradiances (*4, 16, 17*), and therefore greater leaf retention on plants in the shade would be expected, leading to greater LAIs (*18*). The LAI in our study, measured with an electronic canopy analyzer (*19*), increased linearly in all ecosystems during the first 60 days from 3.4 to approximately 7, after which it leveled off (Fig. 1). Steady-state LAI was accompanied by the onset of leaf litter production, which was

Department of Botany, University of Basel, Schönbeinstrasse 6, CH-4056 Basel, Switzerland.

*To whom correspondence should be addressed.